

AN AB INITIO APPROACH TO THE SOLAR CORONAL HEATING PROBLEM

BORIS VILHELM GUDIKSEN¹

The Institute for Solar Physics of the Royal Swedish Academy of Sciences, Albanova University Center,
 Stockholm Observatory, 10691 Stockholm, Sweden; boris@astro.su.se

AND

ÅKE NORDLUND

Astronomical Observatory, NBIAfG, Copenhagen University, Øster Voldgade 3, 1350 Copenhagen K, Denmark;
 aake@astro.ku.dk

Received 2004 January 24; accepted 2004 September 23

ABSTRACT

We present an ab initio approach to the solar coronal heating problem by modeling a small part of the solar corona in a computational box using a three-dimensional MHD code including realistic physics. The observed solar granular velocity pattern and its amplitude and vorticity power spectra, as reproduced by a weighted Voronoi tessellation method, are used as a boundary condition that generates a Poynting flux in the presence of a magnetic field. The initial magnetic field is a potential extrapolation of a *SOHO*/MDI high-resolution magnetogram, and a standard stratified atmosphere is used as a thermal initial condition. Except for the chromospheric temperature structure, which is kept nearly fixed, the initial conditions are quickly forgotten because the included Spitzer conductivity and radiative cooling function have typical timescales much shorter than the time span of the simulation. After a short initial start-up period, the magnetic field is able to dissipate $(3-4) \times 10^6 \text{ ergs cm}^{-2} \text{ s}^{-1}$ in a highly intermittent corona, maintaining an average temperature of $\sim 10^6 \text{ K}$, at coronal density values for which simulated images of the *TRACE* 171 and 195 Å passbands reproduce observed photon count rates.

Subject headings: MHD — Sun: corona — Sun: magnetic fields

1. INTRODUCTION

The heating mechanism at work in the solar corona has puzzled researchers for more than six decades. Several heating mechanisms have been proposed. One of the earliest models involved accretion of interstellar matter coupled with convection in the chromosphere (Bondi et al. 1947), but with improved measurements two main groups of heating models emerged: wave (AC) heating and electric current (DC) heating. These mechanisms move energy from the photospheric kinetic energy reservoir to the internal heat reservoir in the corona through the magnetic field. AC heating (already proposed by Alfvén 1947) depends on the magnetic field being moved around in the solar photosphere faster than the disturbances can propagate through the whole magnetic loop, i.e., faster than the Alfvén crossing time. Only torsional Alfvén waves can reach the corona, while magnetosonic wave modes are diffracted and dissipated because of the strong wave speed gradient in the chromosphere/transition region. Waves have been detected both in the near-Sun corona (see, for instance, Aschwanden 1987; Ofman & Davila 1997) and in the solar wind by a number of spacecraft such as the *Helios 1* and 2 satellites (Neubauer & Musmann 1977), so there is firm evidence for their existence, but not of their ability to supply enough heat. Alfvén waves do not easily dissipate in the corona in the absence of phase mixing (Heyvaerts & Priest 1983) or resonant absorption (Davila 1987), which require strong phase gradients to be efficient.

DC heating relies on motions in the photosphere that change on timescales longer than Alfvén crossing times, allowing the magnetic field to remain close to an equilibrium state. The DC heating mechanism dissipates energy through conventional

Joule heating (proposed by Parker 1972), or reconnection heating (proposed by Glencross et al. 1974, based on X-ray observations) dissipated through flares of all sizes, including nanoflares, or through a hierarchy of current sheets that may encompass both of the above processes (Galsgaard & Nordlund 1996). Until recently, nanoflares appeared to be the most promising candidate, but it now seems that the energy dissipated in the observed flare distribution, extrapolated to a cutoff at nanoflare energies, is too small (Aschwanden et al. 2000c; Parnell & Jupp 2000; Aschwanden & Parnell 2002; Aschwanden & Charbonneau 2002). DC heating has received considerable attention since it was proposed some 30 years ago (e.g., Parker 1972, 1983; Sturrock & Uchida 1981; van Ballegoijen 1986; Mikic et al. 1989; Heyvaerts & Priest 1992; Longcope & Sudan 1994; Galsgaard & Nordlund 1996; Hendrix et al. 1996; Gomez et al. 2000, to mention just a few). It has been established that the DC heating mechanism is feasible, but not to what extent it can provide enough energy to heat the solar corona.

The main problem in modeling solar dissipative processes is the length scales involved. The dissipative length scale is of the order of 1 m for, e.g., a flare with a timescale of the order of 100 s, while the large-scale magnetic field distribution has a scale of many Mm, making fully resolved three-dimensional simulations of such processes practically impossible. However, Parker (1972, 1983) anticipated that the total dissipation would not depend on details of the dissipation mechanism (also discussed in Parker 1979, §§ 6.6.1 and 14). The numerical results of Galsgaard & Nordlund (1996) and Hendrix et al. (1996) indeed showed that the total dissipation only depends very weakly on the resolution and, if anything, increases slightly with increasing resolution (the physical reason behind this perhaps unexpected behavior was pointed out by Parker 1988).²

¹ Current address: Institute of Theoretical Astrophysics, University of Oslo, P.O. Box 1029, Blindern, N-0315 Oslo, Norway; boris@astro.uio.no.

² See page 477, second paragraph in the right-hand column.

It is theoretically possible, since the scaling and normalization has only been verified numerically over a limited range of magnetic Reynolds numbers, that the dissipation level could be different at magnetic Reynolds numbers relevant in the solar case. However, as discussed in detail by Galsgaard & Nordlund (1996), not only the scaling of the dissipation with large-scale parameters, but also the absolute level may be understood as a result of the onset of essentially ideal instabilities at winding numbers from end to end of field lines of the order of unity, and it appears very unlikely that this physically understandable normalization would be lost at large Reynolds numbers. We also point out in this context that the various values of the “critical angle” employed by Parker, e.g., 20° in Parker (1983) and 14° in Parker (1988), were arrived at by working backward from an estimate of the required heating level and then-assumed values of typical velocity amplitudes in the photosphere. See also Dahlburg et al. (2005) for related results.

Results from low-resolution modeling of dissipative processes may thus be used to obtain estimates, or at least to establish *lower* limits on the dissipated energy. This provides the basis for trying to create numerical ab initio simulations of the solar corona, with essentially no free parameters. As discussed in more detail below, the initial and boundary conditions that we use are *minimal assumptions*, in the sense that including more detailed conditions would produce more heating. This allows us to give a firm answer to whether DC heating can provide the energy required and thus which heating mechanism is the principal one in the solar corona.

Initial results of this effort were presented in Gudiksen & Nordlund (2002); here we present further developments, including a realistic photospheric velocity driver and a nonuniform mesh, making it possible to better resolve the density drop in the photosphere and chromosphere and to expand the simulated volume. Details of single loops are presented in a separate paper (Gudiksen & Nordlund 2005), and spectroscopic signatures, such as emission measures, line shifts, and nonthermal line broadening are presented in a third paper (Peter et al. 2004).

2. MODEL

We solve the fully compressible MHD equations on a non-uniform staggered mesh, in the form

$$\frac{\partial \rho}{\partial t} = -\nabla \cdot \rho \mathbf{u}, \quad (1)$$

$$\frac{\partial \rho \mathbf{u}}{\partial t} = -\nabla \cdot (\rho \mathbf{u} \mathbf{u} - \tau) - \nabla P + \mathbf{J} \times \mathbf{B} + \rho \mathbf{g}, \quad (2)$$

$$\mu \mathbf{J} = \nabla \times \mathbf{B}, \quad (3)$$

$$\mathbf{E} = \eta \mathbf{J} - \mathbf{u} \times \mathbf{B}, \quad (4)$$

$$\frac{\partial \mathbf{B}}{\partial t} = -\nabla \times \mathbf{E}, \quad (5)$$

$$\frac{\partial e}{\partial t} = -\nabla \cdot e \mathbf{u} - P \nabla \cdot \mathbf{u} - \nabla \cdot \mathbf{F}_{\text{Spitzer}} + Q_{\text{visc}} + Q_{\text{Joule}} - n_{\text{ion}} n_e \Lambda, \quad (6)$$

where ρ is the mass density, \mathbf{u} is the velocity vector, τ is the viscous stress tensor, P is the gas pressure, \mathbf{J} is the electric current density, \mathbf{B} is the magnetic flux density, \mathbf{g} is the gravitational acceleration, μ is the vacuum permeability, \mathbf{E} is the electric field strength, η is the magnetic diffusivity, e is the internal energy per unit volume, $\mathbf{F}_{\text{Spitzer}}$ is the energy flux due to the Spitzer conductivity (Spitzer 1956) along the magnetic field, Q_{visc} is the viscous heating, Q_{Joule} is the Joule heating, and Λ is the

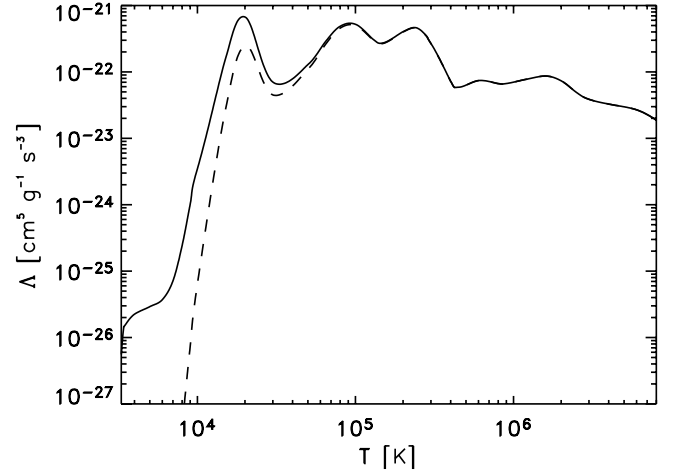


FIG. 1.—Radiative cooling function (*solid line*) and implemented cooling function (*dashed line*) with quenched cooling in the photospheric and chromospheric temperature regimes.

cooling function for the optically thin coronal plasma, with n_{ion} and n_e being the number density of ions and electrons.

The code is explicit and, because of the staggered mesh method, conserves the magnetic divergence to machine precision. The staggered mesh method means that the physical variables are not aligned in space. This is an advantage for the derivative operators, but has the downside that when physical variables at different locations are involved, interpolation is needed to realign the variables. The code uses sixth-order derivative operators and fifth-order interpolation operators, together with a third-order Runge-Kutta time-stepping method with variable time step. The code has been extensively subjected to several standard tests as well as used in several physical regimes, for instance, three-dimensional turbulence and magnetoconvection (Nordlund et al. 1994), magnetic dissipation (Galsgaard & Nordlund 1996), buoyant magnetic flux tubes (Dorch & Nordlund 1998), emergence of flux ropes through the solar convection zone (Dorch et al. 1999), and supersonic MHD turbulence (Padoan & Nordlund 1999).

The computational box of $60 \times 60 \times 37 \text{ Mm}^3$ is resolved on a grid of 150^3 grid points where the vertical scale is non-uniform. The vertical axis starts at the photosphere, with high resolution ($\sim 0.15 \text{ Mm}$) in order to resolve the small pressure scale height in the photosphere and chromosphere. Above the transition region the vertical resolution gradually approaches 0.25 Mm . We acknowledge that the resolution of the transition zone may seem inadequate in comparison to legacy one-dimensional models.

2.1. Radiative Cooling

The cooling function includes the most important transitions for H, He, C, O, Ne, Fe, and bremsstrahlung, with a cutoff at low temperatures to avoid catastrophic cooling in the chromosphere (see Fig. 1). The cooling function is based on the ionization and recombination rates given by Arnaud & Rothenflug (1985) and Shull & van Steenberg (1982) and using the collisional excitation rates found through the HAO-DIAPER Atom data package (Judge & Meisner 1994). The ions are treated by assuming ionization equilibrium, making it possible to derive radiative losses as a function of electron temperature.

Farther down in the atmosphere, where the radiation is optically thick for at least some wavelengths, the cooling processes

cannot be treated with a simple cooling function. The cooling function shown in Figure 1 (*solid line*) uses a cutoff proportional to $\exp(-\tau)$ with the optical depth $\tau \propto P_{\text{gas}}$. In this simulation, the lower part of the chromosphere and the photosphere are instead kept near a fixed average temperature profile using a Newtonian cooling mechanism that forces the local temperature toward a preset function of height on a timescale of about 0.1 s in the photosphere. The timescale increases with decreasing density as $\rho^{-1.67}$, and the effect thus becomes negligible in the corona.

2.2. Boundary Conditions

The vertical boundary conditions are handled by using ghost zones, while the box is periodic in the horizontal directions. The density is extrapolated into the ghost zones, and to prevent heat from leaking into or out of the box, the temperature gradient is set to zero at the upper boundary. The upper boundary is relaxed toward the average temperature at the upper boundary with a typical timescale of about 30 s. The vertical velocity is zero on the boundaries, while the horizontal velocity on the lower boundary is set by a driver (see § 2.3). At the upper boundary the vertical gradient of the horizontal velocity is set to zero and we use a potential field extrapolation for the magnetic field in the ghost zones.

2.3. The Voronoi Tessellation Driver

The solar photospheric velocity field is characterized by granular structures with a range of sizes, from granules with a typical size of ~ 1 Mm to supergranules of size ~ 20 – 30 Mm and even bigger giant cells (Simon & Weiss 1968; Hathaway et al. 2000). These structures have typical velocities that scale with wavenumber roughly as $u \propto k$ and have turnover times of order $\tau \propto k^{-2}$, all the way from beyond supergranular scales to the velocity maximum at granular scales (Stein & Nordlund 1998; Hathaway et al. 2000; Shine et al. 2000). The velocity field injects energy into the magnetic field through a Poynting flux, making a realistic reproduction important.

Our goal was to create a driver that would match these statistical features of the solar velocity spectrum, as well as the geometric features of the granular pattern. The velocity driver is partially based on the theory of *Voronoi tessellation* (see, for instance, Okabe et al. 1992), specifically multiplicatively weighted Voronoi tessellation, inspired by Schrijver et al. (1997a), who showed that this method gives a good fit to observations of the granulation pattern. The theory applied to this case provides a way to split a two-dimensional surface into tiles, each representing a granule. To do this one has to choose a number of generator points, each with a weight w_i (where i represents a specific tile) positioned at \mathbf{x}_i . Tile i then occupies an area where the following inequality is satisfied,

$$\frac{w_i}{|\mathbf{x} - \mathbf{x}_i|} \geq \frac{w_j}{|\mathbf{x} - \mathbf{x}_j|} \text{ for all } j \neq i. \quad (7)$$

To include the intergranular lanes, we increased the complexity of equation (7),

$$\frac{w_i(1 - l_{ig})}{|\mathbf{x} - \mathbf{x}_i|} \geq \frac{w_j}{|\mathbf{x} - \mathbf{x}_j|} < \frac{w_i(1 + l_{ig})}{|\mathbf{x} - \mathbf{x}_i|}. \quad (8)$$

When both conditions are true \mathbf{x} is in an intergranular lane, and where only the left part of the inequality is true \mathbf{x} is in granule i ; l_{ig} is a number between zero and 1 and can be adjusted to make the intergranular area roughly 33%–45% of the total

area (Stein & Nordlund 1998) based on velocity maps. The relative area of the intergranular lanes can be estimated by assuming perfectly round granules,

$$\frac{A_{ig}}{A_{tot}} = 2l_{ig} \frac{(1 - l_{ig})}{(1 + l_{ig})}. \quad (9)$$

2.3.1. The Initial Tessellation

If the generator points were placed randomly there would be both unusually large and unusually small granules generated, because the density of generator points would be low in some places and high in others. Since observed granules are rather uniform in size, only a certain range of sizes of fully grown granules can be accepted. This places restrictions on the placement of the generator points. The tessellation is built up by keeping a list of the weights at each position, independent of whether it is in an intergranular lane or not, updating the list as more granules are placed. In this way a weight function with a value at each position is generated,

$$\mathcal{W}(\mathbf{x}) = \frac{w_i}{|\mathbf{x} - \mathbf{x}_i|}, \text{ where } \frac{w_i}{|\mathbf{x} - \mathbf{x}_i|} \geq \frac{w_j}{|\mathbf{x} - \mathbf{x}_j|} \text{ for all } j \neq i. \quad (10)$$

To generate a new granule, its generator point is placed where the weight function has a value lower than a certain threshold $\mathcal{W}_{\text{thresh}}$. This allows more generator points to be placed only until the weight function is above the threshold at all positions. By choosing an appropriate threshold carefully the density of generator points is such that granules of the right size are created.

The velocity vector points radially away from the generator points inside the granules and along the granular boundaries in the intergranular lanes. The horizontal velocity profile inside mesogranules was modeled by Simon & Weiss (1989) by fitting a simple model to observations done with the SOUP filter on board *Spacelab 2*. The horizontal velocity profiles were successfully fitted with a radial velocity profile of the form $v_h(r) = r \exp[-(r/r_0)^2]$. We found a better fit to the solar velocity power spectrum by using $v_h(r) = r^2 \exp[-(r/r_0)^2]$, giving a flatter profile in the centre of the granules. In the intergranular lanes the velocity is a sum of the velocity of the two granules adjacent to the intergranular lane. Initially this creates stagnation points in the intergranular lanes, on lines connecting the generator points, but such stagnation points disappear when multiple velocity fields are added (see § 2.3.2).

2.3.2. Time Evolution

The tessellation is made time-dependent by making the weights of the generator points time-dependent. We have chosen to give the weights of the generator points a time dependence specified by

$$w_i(t) = W_i \exp\left[-\left(\frac{t - t_{0,i}}{\tau_i}\right)^q\right], \quad (11)$$

where W_i is a constant giving the maximum weight, $t_{0,i}$ is the time of maximum weight, and q is an even integer, indirectly controlling the growth time of the granule. We bring the granule to life when $w_i/dx > \mathcal{W}_{\text{thresh}}$, where dx is the grid resolution, which effectively sets $t_{0,i}$ when W_i is chosen. When $t > t_{0,i}$ the granule is decaying, and it is removed when $w_i/dx < \mathcal{W}_{\text{thresh}}$.

When the weight function $\mathcal{W}(\mathbf{x})$ falls below the threshold in a large connected region, each new granule covers only a small area, causing many small granules to appear, thus making the area crowded with small granules of approximately equal size. This problem is solved by creating a binary function $\mathcal{A}(\mathbf{x}, t)$, which is set to 1 within 80% of the expected radius for granule i at $t = t_{0,i}$ as long as $t \leq t_{0,i}$ and otherwise zero. This region of avoidance keeps new granules from being formed in the immediate vicinity of other newly formed granules. Therefore there are two criteria a new generator point (n) must fulfil when it is generated, in order to be part of the tessellation,

$$\mathcal{W}(\mathbf{x}_n, t) < \mathcal{W}_{\text{thresh}}, \text{ and } \mathcal{A}(\mathbf{x}_n, t) = 0.$$

This ensures that there is room for a new granule and avoids overpopulation of new granules later when the granules are growing. At the same time the weight function evolves such that it makes new granules appear only in intergranular lanes, because this is the location where the weight function first drops below the threshold.

In order to create the velocity-scale relation of the Sun, several granular patterns with different scales must be superposed. This involves creating a number of independent granulation patterns with different typical scales as described above and adding the velocities. We have chosen three layers, with typical granular radii of 1.3, 2.5, and 5.1 Mm, respectively, with velocities and lifetimes following the observed scaling relations. This choice corresponds to sizes ranging from those of large granules to the size of mesogranules and produces on average 880, 280, and 80 granules, respectively, in the three size groups. The smallest scale is set by the resolution, and the largest scale is set by the box size used in the simulation.

Creating the velocity field in this way makes the velocity field ordered on many scales, but also makes it too laminar. The vorticity spectrum from the Voronoi driver is too weak, compared to the simulations of Stein & Nordlund (1998). This has been corrected by using a Helmholtz projection to separate the rotational and irrotational part of the velocity field and then amplifying the rotational part to the same level as in the simulations by Stein & Nordlund (1998).

The velocity is quenched by a factor

$$f_{\text{quench}} = \frac{1 + \beta^{-2}}{1 + 3\beta^{-2}}, \quad (12)$$

depending on the plasma $\beta = P_{\text{gas}}/P_{\text{Mag}}$. In the strongest magnetic field regions the quenching reduces the velocity amplitude by $\sim 60\%$, in order to reproduce the magnetic field's ability to quench convective motions in the Sun.

The velocity-scale relation of the driver, averaged over 45 minutes, is shown in Figure 2. To illustrate the time development of the driver, snapshots of corks flowing in the time-dependent velocity field produced by the driver are shown in Figure 3.

2.4. Initial Conditions

Two initial stratifications were used. The first was taken from the Fontenla-Avrett-Loeser (FAL-C) model (Fontenla et al. 1993) in the photosphere, chromosphere, and transition region, while in the corona a simple isothermal profile with $T = 10^6$ K was used (see Fig. 4). The second was inspired by the work of Carlsson & Stein (see, for instance, Carlsson & Stein 2002), who argue for a highly time-dependent, low mean temperature chromosphere with no average temperature increase. This model has

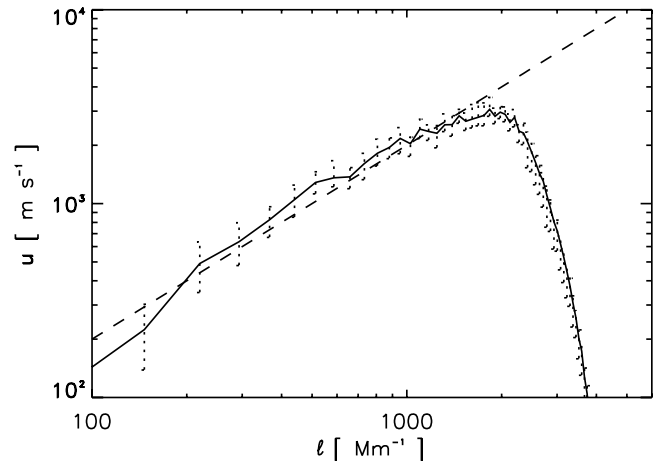


FIG. 2.—Velocity amplitude vs. spherical harmonic wavenumber for the three-layer granulation model (solid line) with the error bars showing maximum deviation through a period of 1 hr. The dashed line shows $u \propto k$.

been criticized by Kalkofen (2001), who argues for a warmer chromosphere. On the other hand, observations of CO by Ayres (2002) point toward an even cooler chromosphere than the one proposed by Carlsson & Stein. The choice of chromospheric model turns out to have only a minor effect on the coronal dynamics and the coronal heating.

To keep the number of free parameters at a minimum, we chose to make the initial magnetic field a potential extrapolation of an observed active region on the Sun. We chose to scale down a high-resolution *SOHO*/MDI observation of NOAA Active Region 9114 from 2000 August 8. The cropped data span 500 pixels \times 500 pixels, corresponding to roughly 225 Mm \times 225 Mm, and was therefore scaled down to fit in the computational box of 60 Mm \times 60 Mm. The distribution of flux on the solar surface seems to be approximately self-similar down to scales ~ 180 km in the network (Schrijver et al. 1997b; Wang et al. 1995), smaller than our resolution. If this also holds in active regions, as seems to be the case (Meunier 2003), this would justify our “rescaling” of the MDI magnetogram. It is, however, necessary to point out that our computational box does not hold an average size solar active region, but at most a small active region, and therefore direct comparisons of these results with larger size active regions should be done with care.

3. RESULTS

The simulation goes through a roughly 5 minute start-up period, where neither thermal conduction nor radiative cooling are turned on. This is related to the magnetic field initial condition. Since the initial magnetic field is potential, it is in a minimum energy state and is therefore initially not able to dissipate any energy. In the first few minutes, thermal conduction and radiative cooling would therefore cool the corona monotonically and make the atmosphere tend to collapse. After the start-up period, when the magnetic field has reached a dissipative state, the radiative cooling and the thermal conduction are turned on. After another approximately 5 minutes solar time a statistical equilibrium is reached, with a nearly time-independent temperature distribution.

3.1. Energy Balance

The thermodynamic equilibrium of the atmosphere is difficult to quantify since the energy fluxes are very intermittent, but

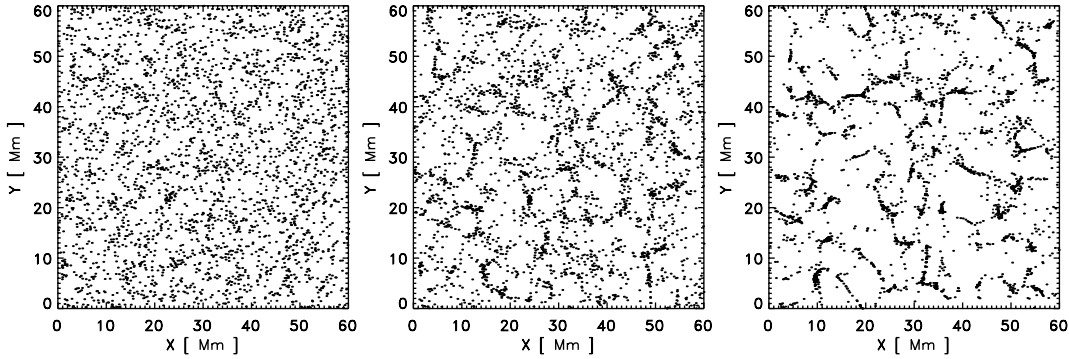


FIG. 3.—Three snapshots of 3000 corks released in the simulated velocity field, without magnetic velocity quenching, at $t = 0$ minutes (left), $t = 15$ minutes (middle), and $t = 45$ minutes (right).

several conclusions may still be drawn from a horizontal average of the energy flux divergences, i.e., the deposited energy. The energy balance is illustrated in Figure 5. This balance is for a typical point in time, and it is obvious that the heating in the corona is decreasing with height, as found from *TRACE* data by a number of authors (Schrijver et al. 1999; Aschwanden et al. 2000a, 2001). The detailed height dependence of the heating in individual loops is investigated in a separate paper (Gudiksen & Nordlund 2005).

It is noteworthy and interesting that the convective flux redistributes as much energy as the Spitzer conductivity does just above the transition region. The heating provided by the magnetic dissipation is transported by the Spitzer conductivity downward from the transition region to the upper chromosphere, where the Spitzer conductivity is no longer effective because of the low temperature. The convective flux removes energy at the same location because of evaporation of chromospheric material into the corona. The energy loss in the lower corona and transition zone due to the Spitzer conductivity is balanced by the heating, which dominates the Spitzer conductivity at larger heights. The optically thin radiative losses go to zero in the lower chromosphere and photosphere because of the quenched radiative cooling function that we adopt. The heating goes to very high values, but in spite of that the temperature stays at chromospheric temperatures because of the Newtonian cooling

with which we represent the complex chromospheric radiation losses at these height. It is not possible to estimate whether any further heating is needed in the chromosphere until we can consistently treat both convective and radiative energy fluxes through the lower boundary, as well as radiative losses in the optically thick lower atmosphere. There should be no major effect on the conclusions drawn about the heating of the transition region and corona due to this inadequacy, because we hold the temperature structure in this region of the Sun close to what it is deduced to be observationally. Incorporating both enthalpy flux and an appropriate treatment of radiation in a nearly ab initio chromospheric model will take a considerable effort, and is a challenge for the future.

3.2. Magnetic Field Configuration and the Dissipative Heating

The energy supplied to the corona originates from the Poynting flux through the lower boundary. In general, magnetic dissipative heating is generated from stressing of the magnetic field. The stressing is largest in the photosphere and low chromosphere, where the plasma β is larger than or of the order of unity in a significant fraction of the volume. At these low heights the magnetic field still has a very intermittent structure, reflecting the intermittent distribution set up by fluid motions in the photosphere and below (represented by the initial and boundary conditions in our numerical model). The plasma β is low in

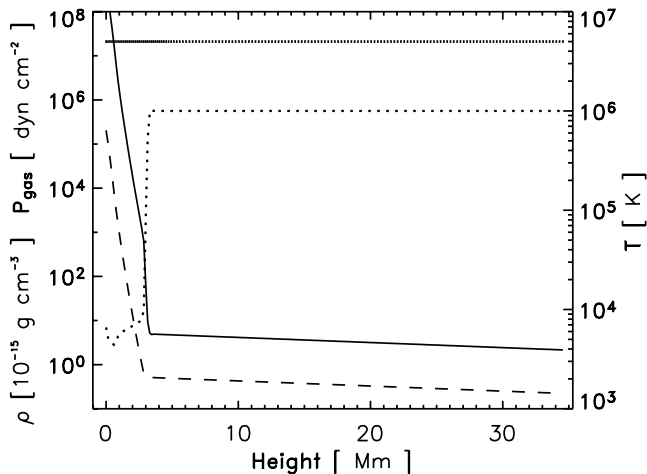


FIG. 4.—Initial stratification for density (solid line), gas pressure (dashed line), and temperature (dotted line). Also shown at the top is the vertical scale, with a small line at each grid point.

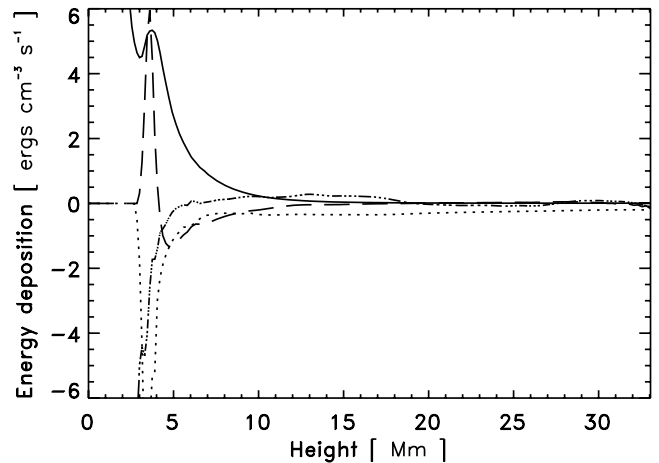


FIG. 5.—Horizontally averaged energy deposition from resistive dissipation (solid line), Spitzer conductivity (long-dashed line), convective flux (dash-dotted line), and radiative cooling (dotted line), as a function of height.

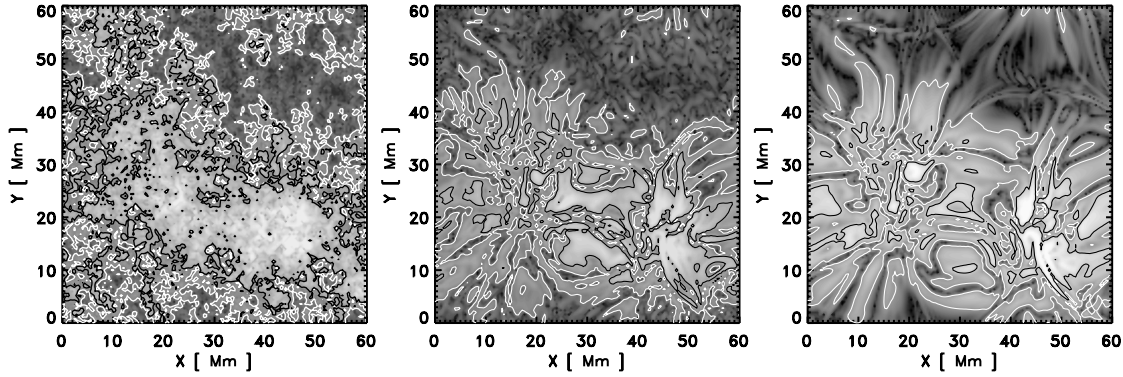


FIG. 6.—Images of the scalar product of electric current and the magnetic field for three different heights in the atmosphere, 0.0, 3.0, and 5.6 Mm, corresponding to photosphere, upper chromosphere, and low corona (left to right). On top are two contours with values a factor of 10 apart (black: high; white: low).

regions with high magnetic field strengths, but is still high in intervening regions with low magnetic field strengths.

In the high chromosphere and above, the magnetic field is nearly space-filling and the plasma β is less than unity almost everywhere (with the exception of small neighborhoods around magnetic null points). The magnetic field thus dominates the dynamics and tends to be “nearly force-free,” in the sense that the Lorentz force is small and the electric currents tend to be nearly parallel with the magnetic field,

$$\mathbf{J} \approx \alpha \mathbf{B}. \quad (13)$$

As is well known and easily proven, α must be constant along each magnetic field line in a truly force-free field, but can certainly vary from one field line to another. Also, since a dynamically evolving coronal magnetic field cannot be entirely force-free, α should not be expected to be exactly constant even along magnetic field lines.

In order to illustrate the variability of α over horizontal planes, Figure 6 shows images of the quantity $|\mathbf{J} \cdot \mathbf{B}| \approx \alpha B^2$ (we prefer to show this quantity rather than $|\mathbf{J} \cdot \mathbf{B}|/B^2$, which would tend to be dominated by regions with low B).

If α was constant these images would effectively be the same as images of B^2 . The actual images show that α varies significantly over horizontal planes, that it varies most rapidly at low heights, and that it certainly cannot be approximated with a constant at any height. The larger horizontal scale of the variability at larger heights is due to the fact that field lines (along which α is at least approximately constant) fan out as they reach higher and hence spread the variability of α over larger patches.

We next comment on the absolute magnitude of α and its consequences for the overall field distribution. Dimensionally, α is an inverse length: the length along a field line over which it twists around itself. As previously established by Galsgaard & Nordlund (1996), field lines that are stressed by a boundary typically are twisted only about once from end to end, corresponding to values of α of the order of $1/L$, where L is the field line length. As illustrated by Figure 6, α is only correlated over small patches near the lower boundary. This implies that the perturbations of the magnetic field line directions must be small (except in special regions such as in the neighborhood of quasi-separatrix layers; Priest & Démoulin 1995), and hence that the overall perturbations of the magnetic field strength distribution, relative to that of a potential field, must also be small. This means that to obtain an overall picture of the

magnetic field strength distribution, a potential field extrapolation is sufficient in cases such as this one, with no large-scale shear.

We expect the heating to generally be proportional to the electric current squared, and if the field is in a nonlinear force-free state we also expect the electric current squared and thus the heating to be proportional to the magnetic field strength squared. Figure 7 shows a contour plot of the distribution of heating with height in the atmosphere. One can see that the heating is largest at low heights because of the stressing of the magnetic field in a high- β environment. Through the photosphere and chromosphere it declines by some 4 orders of magnitude before reaching the transition region, above which the magnetic field is nearly force free and the heating is indeed approximately proportional to the magnetic field strength squared. Even though the electric current is highly intermittent in horizontal planes, the current relative to the magnetic field strength is almost constant along field lines above the transition region, as is to be expected when α is constant along magnetic field lines. Heating with these characteristics was proposed by Schrijver et al. (1999) and later deduced with data from TRACE by Aschwanden et al. (2001). Further studies of heating models and observations have all supported these heating function characteristics (Mandrini et al. 2000; Foley et al.

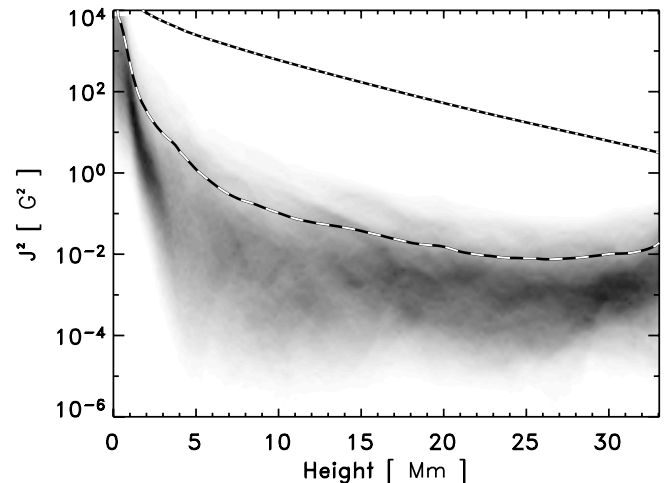


FIG. 7.—The pdf of the electric current squared as a function of height; dark colors mean higher pdf with logarithmic color table. Overplotted is the horizontal average of the magnetic field squared (dotted line) and the horizontal average of the current squared (dashed line).

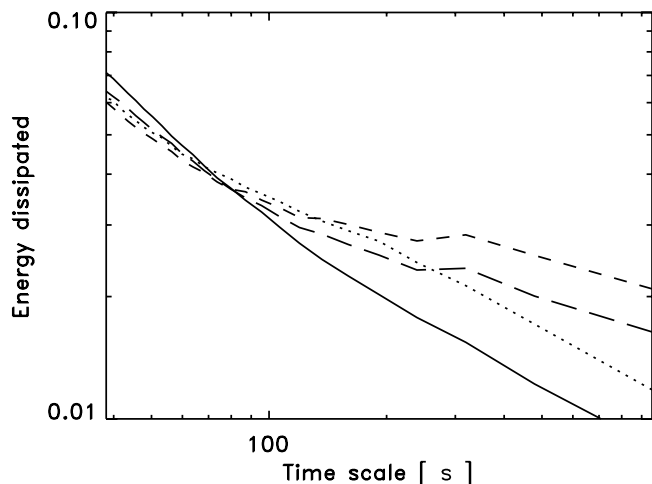


FIG. 8.—Dissipated energy as function of timescale in the upper chromosphere (*solid line*), transition region (*long-dashed line*), lower corona (*dashed line*), and upper corona (*dotted line*) in arbitrary units. The curves are normalized at the maximum timescale.

2002; Schrijver & Aschwanden 2002; Démoulin et al. 2003; Schmieder et al. 2003).

The time variability of the heating depends critically on height. Figure 8 shows on which timescales the energy dissipation varies, calculated as $k_t \sqrt{P_e}$, where k_t is the time-wavenumber and P_e is the power spectrum of the dissipated energy as a function of time at each point. This produces a plot showing on what timescales the energy is dissipated. The energy dissipated is normalized to the total amount of dissipated energy. Without this normalization the curves would be widely spaced along the y -axis because of the exponential decrease in total dissipated energy with height. In general, most of the energy is dissipated as short-timescale events. In the upper chromosphere, the energy comes primarily from events with a timescale shorter than the time resolution of our snapshot data set (~ 38 s). Slightly farther up into the corona, the fraction of energy dissipated at short timescales is less pronounced. The rapid events most likely correspond to “nanoflare”-like reconnection events. With increasing spatial resolution, we would expect to resolve smaller and smaller and hence increasingly more short-lived events.

The energy supplied by the Poynting flux is distributed initially between changes of kinetic, thermal, potential and magnetic energy, and dissipation. After the system has settled into a statistical equilibrium, the energy is only used to compensate for magnetic and kinetic dissipation. The energy is dissipated in the whole atmosphere, with the main part in the photosphere and chromosphere. The Poynting flux at the lower boundary is highly intermittent, but the total Poynting flux is close to constant. Comparing the flux of energy through the lower boundary and the heating rate in the corona gives an overall energy conversion “efficiency.” The time evolution of the efficiency is shown in Figure 9 (*solid line*) during a 20 minute period. During this time the numerical resistivity was changed several times, apparently without significant effect on the efficiency (see the figure caption for details). The efficiency is in the range 5%–10%. That the changes in resistivity have little effect both on the Poynting flux into the system and on the efficiency is consistent with the results of Hendrix et al. (1996) and Galsgaard & Nordlund (1996). The radiative losses of the corona are in the range 1%–3% during the same time period (Fig. 9, *dashed*

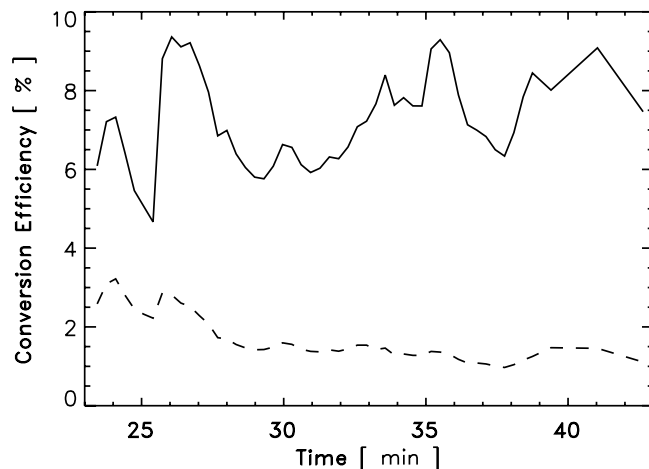


FIG. 9.—Energy conversion efficiency as a function of time during a 23 minute period. The relative amount of energy converted into heating (*solid line*) and the relative amount of energy lost to radiation (*dashed line*) in the corona are shown. The resistivity was increased by a factor of 2.5 relative to the initial value at $t \approx 6.7$, was reduced with 20% at $t \approx 22.8$, and was returned to the initial value at $t \approx 25.4$.

line), making it less important than the Spitzer conductivity, as expected.

The total amount of heating needed in active regions has been estimated several times based on UV and X-ray fluxes and typically gives values in the range 10^6 – 10^7 ergs $\text{cm}^{-2} \text{s}^{-1}$. These values are in general hard to estimate precisely, since the total area of the active region can be chosen based on different criteria. Figure 10 shows the average dissipated energy per second and square centimeter in our model, in gas that is emitting UV and X-rays ($T > 5 \times 10^5$ K), in volumes below which the photospheric magnetic field is higher than a certain threshold. If only regions with high magnetic field strength below them are taken into account, the average energy dissipation can be as high as 8×10^6 ergs $\text{cm}^{-2} \text{s}^{-1}$, while if one includes areas with lower field strengths the average dissipation rate declines, but remains above 2×10^6 ergs $\text{cm}^{-2} \text{s}^{-1}$ for the field strengths shown in Figure 10. These values of the average heating are well within the observational limits. The total energy dissipated if the chromosphere and transition region are also included is

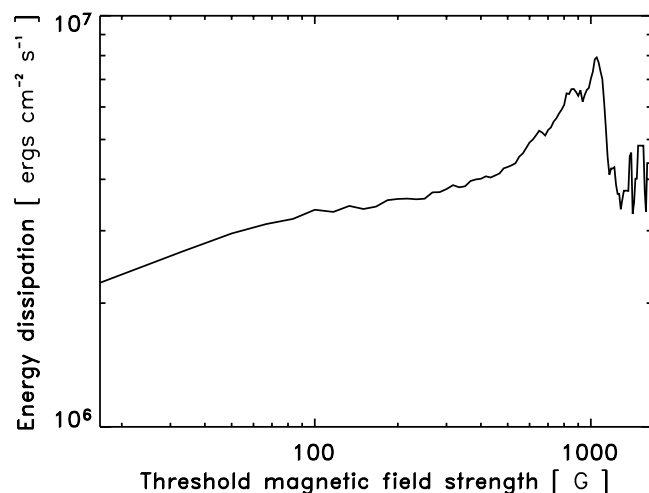


FIG. 10.—Average heating rate in UV to X-ray emitting gas as a function of the underlying photospheric magnetic field strength threshold.

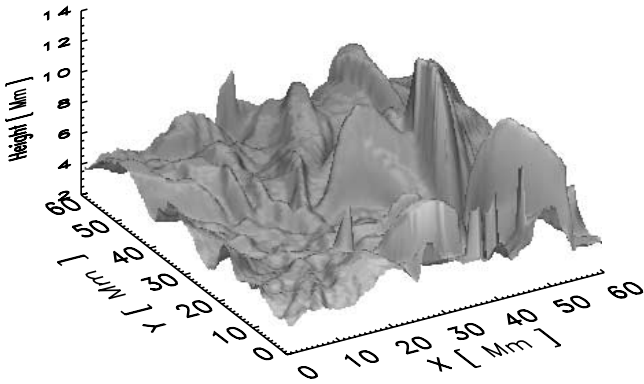


FIG. 11.—Surface showing the height of the transition region, defined as where the temperature rises above 10^5 K.

substantially larger than these numbers, because most of the energy is dissipated in the high field strength environment of the lower atmosphere.

3.3. Stratification

As limb observations by *TRACE* have indicated for some time (Schrijver & McMullen 1999; A. M. Title & C. J. Schrijver 2003, private communication), the transition region does not occur at a well-defined height. The variation in transition region height, defined in our model as the height where the temperature rises above 10^5 K, is shown in Figure 11 for one of the snapshots. The height above the photosphere varies from 2.7 to 12.3 Mm, with an average of 5.0 Mm, and changes over small distances. In spite of the short cooling time in the chromospheric layers, the intermittent heating is able to change the temperature profile in the chromosphere. The intermittency of the height of the transition region is thus a result of intermittent heating at all depths, which causes variations in the chromospheric and coronal temperature and pressure profiles.

The stratification of the corona is intermittent on even the smallest scales. The temperature is generally around 1 MK, but there are large deviations from this average temperature. There are differences in temperature of up to 0.7 MK over distances comparable to *TRACE*'s pixel size (~ 375 km). The temperature gradients are most likely limited by the numerical resolution and are therefore only lower limits. Because of the large temperature gradients, modeling coronal loops as monolithic structures cannot be a good approximation, thus making multithread models of loops called for (Aschwanden et al. 2000b).

Figure 12 shows that even at large heights in the corona there is gas at low temperatures. Evidence for cool gas suspended in the corona has been found through limb observations with *TRACE* based on opacity estimates (Schrijver & McMullen 1999; Schrijver et al. 1999). The cool dense material in the lower part of the corona are primarily surges of chromospheric material that flow into the corona, or condensations of coronal material on its way down. Higher up in the corona it is typically gas undergoing catastrophic cooling (Schrijver 2001). At times surges of material happen simultaneously in both footpoints of a loop, which brings large amounts of material to the top of the loop. If the loop is inclined relative to the vertical, accumulated mass at its top can force the loop top down and make it almost horizontal along part of its length, thus suspending the cold material in the corona. An example is the large structure at roughly $(x, y) = (40, 25)$ in Figure 11, which has a horizontal column density of up to $6 \times 10^{20} \text{ cm}^{-2}$ at a height of 8.0 Mm, making it a

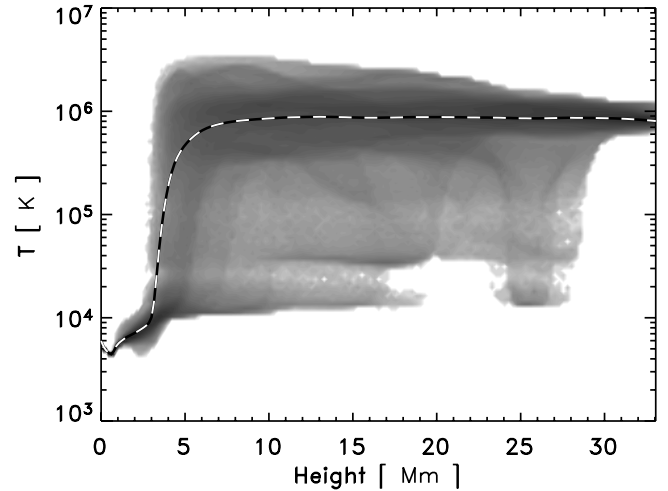


FIG. 12.—Histogram of the temperature pdf for each height for the FAL-C chromosphere. Dark is high pdf, with a logarithmic gray scale. The horizontal average is overplotted (dashed line).

visible absorbing structure for UV at the limb. The structure is long lived, having existed for 10 minutes at the end of the simulation sequence. There are other similar structures, but too few to give a basis for firm estimates of typical characteristics.

The density has values that vary by at least 2 orders of magnitude in the corona, over any horizontal slice. The average density and temperature in the corona depend primarily on the amount of Poynting flux reaching the corona, which in turn depends on the amount injected through the lower boundary and the amount that is dissipated in the photosphere and chromosphere. The horizontal variations of density and temperature primarily reflect the variations of properties from loop to loop. In general, the highest densities are in loop structures with low temperatures, persisting all the way to the top of the atmosphere. A two-dimensional histogram of the probability density function (pdf) of the density at each height for the FAL-C chromosphere is displayed in Figure 13, which shows that the horizontally averaged density stays almost constant through the part of the corona that we model, with an average number density close to 10^9 cm^{-3} , but with values ranging from 10^8 to a

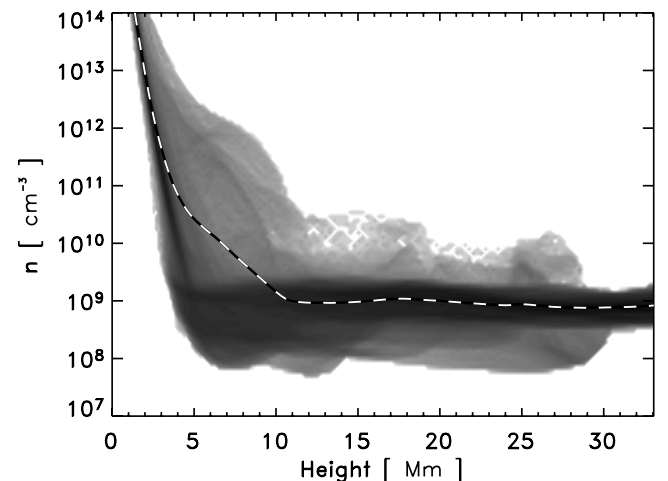


FIG. 13.—Histogram of the density pdf for each height for the FAL-C chromosphere. Dark is high pdf, with a logarithmic gray scale. The horizontal average for the distribution is overplotted (dashed line).

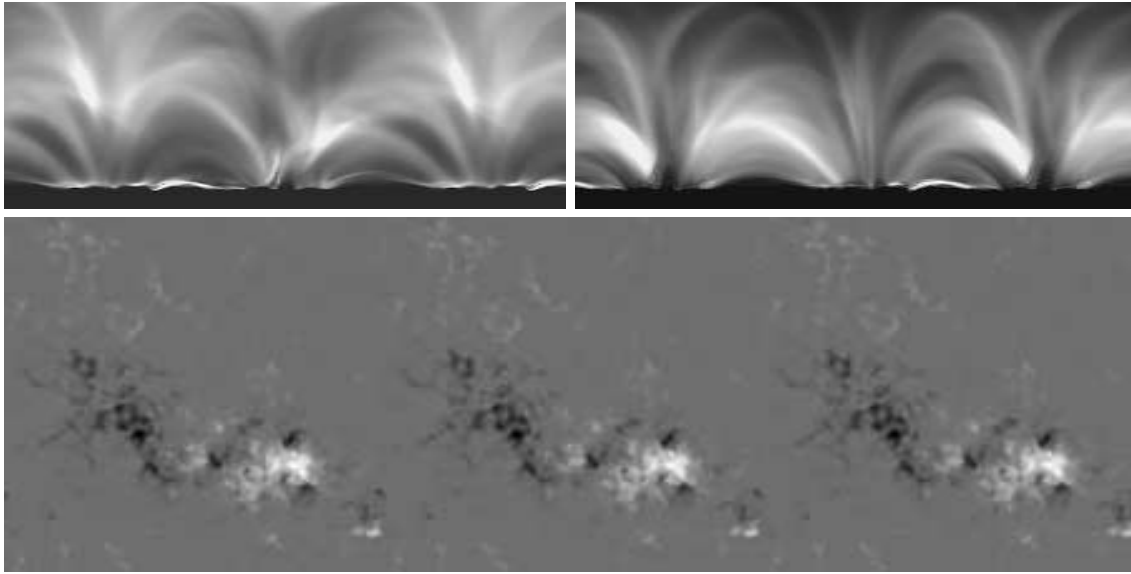


FIG. 14.—Emulated *TRACE* 171 (top left) and 195 (top right) images both spanning 1.5 box lengths, and the underlying photospheric magnetic field.

few times 10^{10} cm^{-3} , typical of or slightly higher than observed for active region loops (see, for instance, Mason et al. 1999).

The velocities in the corona are not completely field aligned. In the lower corona 80% of the velocity amplitude is mostly along the magnetic field, whereas higher in the corona the fraction drops to roughly 50%. In the lower corona the strong field regions have velocities that are almost fully field aligned, while the lower field strength regions have less prevalence for velocities along the magnetic field. In the upper corona the velocities are no longer strongly correlated with the magnetic field, and the velocities perpendicular to the magnetic field are now as strong as those aligned with the magnetic field. The cross-field velocities represent bulk motion of the field and the plasma, rather than diffusion across the magnetic field. In general, the velocity amplitudes in the corona are largest just above the transition region, where the impulsive energy releases can accelerate plasma to high velocities. Velocities in this region reach as high as 400 km s^{-1} but with an average of only a few tens of km s^{-1} .

3.4. *TRACE* Emission Measure

Direct comparison of actual photon count rates between *TRACE* observations and these simulations is complicated for several reasons. Del Zanna & Mason (2003) pointed out that the temperature response functions of the *TRACE* filters are based on the Chianti (ver. 2.0) database (Landi et al. 1999), which does not include recombinations to and transitions for Fe VIII, and this affects the response functions somewhat. Several ionization equilibria models are published (see, for instance, Mazzotta et al. 1998; Arnaud & Raymond 1992; Arnaud & Rothenflug 1985), with differences that can give changes in the response function by up to a factor of 2 (G. Del Zanna & H. E. Mason 2003, private communication). In the current work we have used the *TRACE* response function by Del Zanna & Mason (2003), with the ionization states of Mazzotta et al. (1998) and the elemental abundances by Feldman (1992), calculated at a constant electron pressure of $10^{15} \text{ K cm}^{-2}$. We have also made calculations using the local electron pressure instead of a constant electron pressure and found that the difference is minor (typically less than 10%), but the calculations are much more computationally expensive.

The images in Figure 14 have been produced by folding the temperatures and densities of the simulation with the response function. In the run with the FAL-C chromosphere the calculated intensities in the *TRACE* 171 and 195 filters are between 60–70 and 15–25 $\text{DN s}^{-1} \text{ pixel}^{-1}$. For individual loops chosen from the simulated *TRACE* 171 image, that is too high by almost a factor of 10 for the 171 filter and a factor of 3 for the 195 filter, compared to the values given by Del Zanna & Mason (2003). There are several possible explanations for this discrepancy. The images show a forest of loops of all heights. Some of the loops appear broad and diffuse, but this is often an effect of the perspective: most of these broad loops are not connected along the projected axis. The numbers in Del Zanna & Mason (2003) are for a single, well-isolated, high-reaching loop, while the large number of loops in the emulated images often are hard to isolate. The maximum coronal loop height in the current model is limited to $\sim 30 \text{ Mm}$; loops penetrating the upper boundary are not reliable, since the boundary conditions cannot rigorously model the effects of the loop top on the part of the loop included in the box. The count rates are therefore hard to compare directly. The difference in the count rates in the two filters indicates that there is lack of high-temperature material. Based on the previous work by Galsgaard & Nordlund (1996), we expect that higher resolution will create more intermittent structures, creating a broader range of temperatures and effectively shifting gas out of the 171 and 195 filters. Cross sections and other properties of individual loops are examined in a separate paper (Gudiksen & Nordlund 2005).

4. CONCLUSION

The increase in computer performance and system memory in recent years has made it possible to approach the solar coronal heating problem from a new angle. Previously mainly qualitative models have been developed, with assumptions of the magnetic field structure and/or the atmospheric stratification that necessarily have been simplified. This has kept conclusions about the underlying processes indecisive. Observational results from the *SOHO* and *TRACE* satellites have been able to put constraints on the overall heating function, favoring a heating function decreasing exponentially with height (Schrijver

et al. 1999; Aschwanden et al. 2000a, 2001). Observations of nano- and microflares seem to indicate that even if one extrapolates the distributions down to energies that are unobservable, they are not able to supply all the energy needed (Aschwanden & Charbonneau 2002; Aschwanden & Parnell 2002; Parnell & Jupp 2000).

By performing direct numerical simulations we have been able to show that moving footpoints of the magnetic field around in a way consistent with the observed solar photospheric velocity fields inevitably leads to an amount of energy dissipation in the corona that is comfortably within the observational limits. The approach is nearly *ab initio*, using only observed facts, such as the average velocity field properties, a realistic active region photospheric magnetic field, a realistic optically thin cooling function, and Spitzer conductivity.

As anticipated by Parker (1972), and as demonstrated numerically by Galsgaard & Nordlund (1996) and Hendrix et al. (1996), because of copious current sheet generation the magnetic dissipation depends only weakly on the conductivity (here determined by the numerical resolution). This is also in line with other work on three-dimensional reconnection (Biskamp 1993, chap. 6). If anything, it *increases* slightly as smaller scales are resolved, consistent with arguments by Parker (1983), in that the amount of Poynting flux injected through the lower boundary depends on the average angle between the magnetic field direction and the vertical. A larger than solar resistivity may produce a somewhat smaller typical angle, resulting in a smaller value for the Poynting flux. Thus, the current simulation, if anything, underestimates the injected Poynting flux, in line with the *ab initio* approach.

An aspect that *will* depend on numerical resolution, however, is the time variability and intermittency of the heating. As demonstrated by Galsgaard & Nordlund (1996), the hierarchy of current sheets in which the magnetic dissipation takes place extends to ever smaller size as the numerical resolution is increased. It is presumably the intrinsic time variability from the reconnection events in this hierarchy that gives rise to the flare event size power-law distribution. From this point of view, there is no conflict between the current model and the observations that have inspired the nanoflare coronal heating models.

The main results of the coronal modeling is that the total dissipated energy is within the observational limits, making this heating mechanism at least a major constituent (and an unavoidable one!) in heating the solar corona. The energy release should at least partially be observable as a distribution of flare-like events (Galsgaard & Nordlund 1996), but we cannot yet estimate the fraction of the energy released in the form of nanoflares, or predict their energy distribution, since this requires much higher numerical resolution.

The magnetic field is in two distinctly different states, above and below the height where the $\beta = 1$ layer is located. Below, the field is controlled by the photospheric gas motions and is in general in a nonrelaxed state. The magnetic field there dissipates energy at a high rate, since the magnetic energy density is high, the magnetic field lines are short, and since oppositely directed field lines may be forced toward each other without the magnetic pressure having a dominant effect on the total pressure.

In the present simulations roughly 90% of the total dissipated energy is dissipated below the transition region. Above the transition region the magnetic field assumes a nonlinear, nearly force-free configuration, where the dissipated energy is roughly proportional to the magnetic energy density. Several observations point toward a heating function with precisely these

properties (Mandrini et al. 2000; Foley et al. 2002; Schrijver & Aschwanden 2002; Démoulin et al. 2003; Schmieder et al. 2003).

The results for the distribution of both temperature and density are also well within the observed values, even though these values might change slightly depending on the stratification of the upper chromosphere. The temperature is intermittent on the smallest scales, changing by as much as 0.7 MK on the scale of a *TRACE* pixel size. The temperature has values from 10^4 to 3×10^6 K in most of the corona, with a transition zone defined as being at temperatures near 5×10^5 K and varying by as much as 9 Mm in height, similar to what has been inferred from *TRACE* observations (Schrijver & McMullen 1999; A. M. Title & C. J. Schrijver 2003, private communication). The average density is almost constant with height in the corona, but has values at each height spanning 2 orders of magnitude.

From the point of view of the energy balance, the density and temperature in the corona play different but tightly coupled roles. On the one hand, the radiative cooling function changes relatively little with temperature, from a few times 10^5 K to a few times 10^6 K, while the cooling per unit volume is proportional to the square of the density. On the other hand, heat conduction scales as $T^{7/2}$, but any increase in heat conduction also results in more evaporation from the chromosphere and so tends to increase the density in the corona. So in this sense the temperature is not by itself a sensitive probe for the heating in the corona but has to be taken together with density information, and with information about the temperature gradients along the magnetic field. We remark that the temperature gradients in the transition region are only marginally resolved by these simulations. This may affect the heat conduction and details of the energy balance just above the transition region at locations with a sharp temperature gradient.

Making a direct comparison with *TRACE* observations of an active region is hampered by both the question of the statistical significance of a single observation and by the insufficient knowledge of the ionization balance in the corona that makes computed photon count rates uncertain by up to a factor of 2. In spite of these difficulties the emission measures in the *TRACE* 171 and 195 Å bands estimated from the simulations are not far from observed values. The discrepancies (mainly too much emission in the 171 band) are most likely due to missing intermittency, in turn due to the limited numerical resolution. As discussed in the previous section, increased numerical resolution is expected to give a broader distribution of temperatures, reaching higher peak values. This will reduce the emission measure in the 171 band and will also affect the 195 band.

To reproduce the hotter *Yohkoh* loops will require a temperature distribution that extends to higher values than what we find here. Increased heating will inevitably result if a more complete representation of the solar velocity field is used. In the current simulations there is a resolution cutoff in the velocity driving toward smaller scales, and a box size cutoff toward larger scales. It is interesting to note that scaling expressions for coronal heating predict that the heating should scale with the product of the velocity amplitude and the size scale of the motions, so there should be significant additional heating from larger scales. However, with the turnover time varying roughly as the square of the scale of motions, it will take an ever-increasing amount of computer capacity to recover these contributions from larger scale motions.

A more accessible but less well defined contributor to additional heating would be active region-specific velocity fields, such as shearing motions and sunspot rotation. Such systematic

motions would cause systematically stressed magnetic fields, producing locally enhanced heating rates in areas affected by the additional systematic motions. Emerging flux is another contributor to heating that is not treated in this simulation but that happens continuously on the Sun and will produce additional heating if included.

B. V. G. acknowledges support through an EC-TMR grant to the European Solar Magnetometry Network. The work of Å. N.

was supported in part by the Danish Research Foundation, through its establishment of the Theoretical Astrophysics Center. Computing time was provided by the Swedish National Allocations Committee and by the Danish Center for Scientific Computing. The authors thank G. Del Zanna for the improved *TRACE* response function, R. Nightingale for general help with the *TRACE* characteristics, and V. Hansteen for providing the radiative cooling function. Both authors gratefully acknowledge the hospitality of LMSAL and ITP/UCSB (through NSF grant PHY 99-07949) during this work.

REFERENCES

- Alfvén, H. 1947, *MNRAS*, 107, 211
 Arnaud, M., & Raymond, J. 1992, *ApJ*, 398, 394
 Arnaud, M., & Rothenflug, R. 1985, *A&AS*, 60, 425
 Aschwanden, M. J. 1987, *Sol. Phys.*, 111, 113
 Aschwanden, M. J., & Charbonneau, P. 2002, *ApJ*, 566, L59
 Aschwanden, M. J., Nightingale, R. W., & Alexander, D. 2000a, *ApJ*, 541, 1059
 ———. 2000b, *ApJ*, 541, 1059
 Aschwanden, M. J., & Parnell, C. E. 2002, *ApJ*, 572, 1048
 Aschwanden, M. J., Schrijver, C. J., & Alexander, D. 2001, *ApJ*, 550, 1036
 Aschwanden, M. J., et al. 2000c, *ApJ*, 535, 1047
 Ayres, T. R. 2002, *ApJ*, 575, 1104
 Biskamp, D. 1993, *Nonlinear Magnetohydrodynamics* (Cambridge: Cambridge Univ. Press)
 Bondi, H., Hoyle, F., & Lyttleton, R. A. 1947, *MNRAS*, 107, 184
 Carlsson, M., & Stein, R. F. 2002, *ApJ*, 572, 626
 Dahlburg, R. B., Klimchuk, J. A., & Antiochos, S. K. 2005, *ApJ*, in press
 Davila, J. M. 1987, *ApJ*, 317, 514
 Del Zanna, G., & Mason, H. E. 2003, *A&A*, 406, 1089
 Démoulin, P., van Driel-Gesztelyi, L., Mandrini, C. H., Klimchuk, J. A., & Harra, L. 2003, *ApJ*, 586, 592
 Dorch, S. B. F., Archontis, V., & Nordlund, Å. 1999, *A&A*, 352, L79
 Dorch, S. B. F., & Nordlund, Å. 1998, *A&A*, 338, 329
 Feldman, U. 1992, *Phys. Scr.*, 46, 202
 Foley, C. R., Patsourakos, S., Culhane, J. L., & MacKay, D. 2002, *A&A*, 381, 1049
 Fontenla, J. M., Avrett, E. H., & Loeser, R. 1993, *ApJ*, 406, 319
 Galsgaard, K., & Nordlund, Å. 1996, *J. Geophys. Res.*, 101, 13445
 Glencross, W. M., Dorling, E. B., & Herring, J. R. H. 1974, *Sol. Phys.*, 38, 183
 Gomez, D. O., Dmitruk, P. A., & Milano, L. J. 2000, *Sol. Phys.*, 195, 299
 Gudiksen, B. V., & Nordlund, Å. 2002, *ApJ*, 572, L113
 ———. 2005, *ApJ*, 618, 1031
 Hathaway, D. H., et al. 2000, *Sol. Phys.*, 193, 299
 Hendrix, D. L., van Hoven, G., Mikic, Z., & Schnack, D. D. 1996, *ApJ*, 470, 1192
 Heyvaerts, J., & Priest, E. R. 1983, *A&A*, 117, 220
 ———. 1992, *ApJ*, 390, 297
 Judge, P. G., & Meisner, R. 1994, in *Proc. Third SOHO Workshop: Solar Dynamic Phenomena and Solar Wind Consequences*, ed. J. J. Hunt & V. Domingo (ESA SP-373; Paris: ESA), 67
 Kalkofen, W. 2001, *ApJ*, 557, 376
 Landi, E., Landini, M., Dere, K. P., Young, P. R., & Mason, H. E. 1999, *A&AS*, 135, 339
 Longcope, D. W., & Sudan, R. N. 1994, *ApJ*, 437, 491
 Mandrini, C. H., Démoulin, P., & Klimchuk, J. A. 2000, *ApJ*, 530, 999
 Mason, H. E., Landi, E., Pike, C. D., & Young, P. R. 1999, *Sol. Phys.*, 189, 129
 Mazzotta, P., Mazzitelli, G., Colafrancesco, S., & Vittorio, N. 1998, *A&AS*, 133, 403
 Meunier, N. 2003, *A&A*, 405, 1107
 Mikic, Z., Schnack, D. D., & van Hoven, G. 1989, *ApJ*, 338, 1148
 Neubauer, F. M., & Musmann, G. 1977, *J. Geophys. Res.*, 82, 3201
 Nordlund, Å., Galsgaard, K., & Stein, R. F. 1994, in *Solar Surface Magnetism*, ed. R. J. Rutten & C. J. Schrijver (NATO ASI Ser. C., 433; Dordrecht: Kluwer), 471
 Ofman, L., & Davila, J. M. 1997, *ApJ*, 476, L51
 Okabe, A., Boots, B., & Sugihara, K. 1992, *Spatial Tesselations: Concepts and Applications of Voronoi Diagrams* (New York: Wiley)
 Padoan, P., & Nordlund, Å. 1999, *ApJ*, 526, 279
 Parker, E. N. 1972, *ApJ*, 174, 499
 ———. 1979, *Cosmical Magnetic Fields: Their Origin and Their Activity* (Oxford: Clarendon)
 ———. 1983, *ApJ*, 264, 642
 ———. 1988, *ApJ*, 330, 474
 Parnell, C. E., & Jupp, P. E. 2000, *ApJ*, 529, 554
 Peter, H., Gudiksen, B. V., & Nordlund, Å. 2004, *ApJ*, 617, L85
 Priest, E. R., & Démoulin, P. 1995, *J. Geophys. Res.*, 100, 23443
 Schmieder, B., Rust, D., Georgoulis, M., & Bernasconi, P. 2003, abstract in *IAU Symp. 219, Stars as Suns: Activity, Evolution and Planets*, ed. A. Title & K. Schrijver (Dordrecht: Kluwer)
 Schrijver, C. J. 2001, *Sol. Phys.*, 198, 325
 Schrijver, C. J., & Aschwanden, M. J. 2002, *ApJ*, 566, 1147
 Schrijver, C. J., Hagenaar, H. J., & Title, A. M. 1997a, *ApJ*, 475, 328
 Schrijver, C. J., & McMullen, R. A. 1999, *BAAS*, 31, 964
 Schrijver, C. J., Title, A. M., van Ballegoijen, A. A., Hagenaar, H. J., & Shine, R. A. 1997b, *ApJ*, 487, 424
 Schrijver, C. J., et al. 1999, *Sol. Phys.*, 187, 261
 Shine, R. A., Simon, G. W., & Hurlburt, N. E. 2000, *Sol. Phys.*, 193, 313
 Shull, J. M., & van Steenberg, M. 1982, *ApJS*, 48, 95
 Simon, G. W., & Weiss, N. O. 1968, *Z. Astrophys.*, 69, 435
 ———. 1989, *ApJ*, 345, 1060
 Spitzer, L. 1956, *Physics of Fully Ionized Gases* (New York: Wiley)
 Stein, R. F., & Nordlund, Å. 1998, *ApJ*, 499, 914
 Sturrock, P. A., & Uchida, Y. 1981, *ApJ*, 246, 331
 van Ballegoijen, A. A. 1986, *ApJ*, 311, 1001
 Wang, J., Wang, H., Tang, F., Lee, J. W., & Zirin, H. 1995, *Sol. Phys.*, 160, 277

ERRATUM: “AN AB INITIO APPROACH TO THE SOLAR CORONAL HEATING PROBLEM”
(ApJ, 618, 1020 [2005])

BORIS VILHELM GUDIKSEN

The Institute for Solar Physics of the Royal Swedish Academy of Sciences, Sweden

AND

ÅKE NORDLUND

Astronomical Observatory, Copenhagen University, Denmark

Because of an error at the Press, an incorrect version of Figure 5 was published, in which what should be a dash-dotted line (showing convective flux) appears as a solid line. The correct version appears below. The Press sincerely regrets the error.

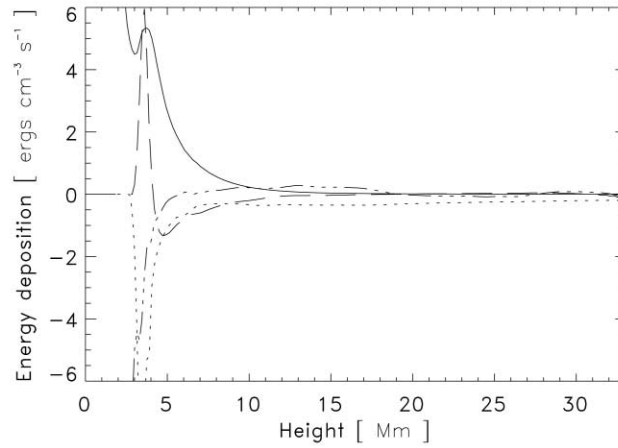


FIG. 5.—Horizontally averaged energy deposition from resistive dissipation (*solid line*), Spitzer conductivity (*long-dashed line*), convective flux (*dash-dotted line*), and radiative cooling (*dotted line*), as a function of height.